Analysis of dynamical processes using the mass distribution of fission fragments in heavy-ion reactions

Y. Aritomo

Flerov Laboratory of Nuclear Reactions, JINR, Dubna, Russia and Japan Atomic Energy Agency, Tokai, Ibaraki, 319-1195, Japan

(Received 26 August 2009; published 4 December 2009)

We analyze experimental data obtained for the mass distribution of fission fragments in the reactions $^{36}S + ^{238}U$ and $^{30}Si + ^{238}U$ at several incident energies, which were performed by the Japan Atomic Energy Agency (JAEA) group. The analysis of the mass distribution of fission fragments is a powerful tool for understanding the mechanism of the reaction in the heavy and superheavy-mass regions. Using the dynamical model with the Langevin equation, we precisely investigate the incident energy dependence of the mass distribution of fission fragments. This study is the first attempt to treat such experimental data systematically. We also consider the fine structures in the mass distribution of fission fragments caused by the nuclear structure at a low incident energy. It is explained why the mass distribution of fission fragments has different features in the two reactions. The fusion cross sections are also estimated.

DOI: 10.1103/PhysRevC.80.064604 PACS number(s): 25.70.Jj, 24.60.Ky, 25.60.Pj, 27.90.+b

I. INTRODUCTION

The aims of the research of nuclei in the superheavy-mass region are to find new magic numbers next to $Z = 82$ and $N = 126$ and to verify the existence of the "Island of Stability" [1]. Moreover, such investigations resulted in the discovery of new elements [2–4]. In the superheavy-mass region, since the fission barrier of the liquid drop model is zero or almost zero, the effect of shell-correction energy is pronounced. The estimated shell-correction energies at the ground state and the fission barrier heights are strongly connected to the stability of superheavy elements.

In a heavy-ion reaction, the shell-correction energy affects the dynamics of the fusion-fission process at a low incident energy. When colliding partners have a strong shell structure the fusion probability is increased [5,6]. In a cold fusion reaction with a Pb or Bi target [3,4] it is recognized that the effect of the nuclear structure leads to a compound nucleus [7,8]. Among the fission fragments obtained from the reaction with ^{48}Ca projectile and actinide targets there are some enhanced productions at or close to the magic nuclei Pb or Sn [9]. These facts suggest that the shell structure plays an important role in the low-energy fusion-fission process in the superheavy-mass region. In addition, in the fusion reaction using an actinide target, the deformation of the nuclei affects the fusion probability [10,11].

In such nuclear collisions, we can observe various types of reactions simultaneously, for example, deep-inelastic collision (DIC), quasifission (QF) reaction, fusion-fission (FF) reaction, and the production of the evaporation residue (EVR) nuclei. The clarification of these mechanisms is very important for obtaining an overall understanding of the reaction processes. Moreover, such studies are strongly connected to the synthesis of new elements.

The evaporation residue cross section of superheavy elements is extremely small. Nevertheless, a large amount of experimental data is available, including the mass and total kinetic energy (TKE) distributions of fission fragments, angle distribution, charge distribution, and prescission neutron multiplicity. First, using a lot of available experimental data, we verify the validity of our model and establish a reliable model to describe the fusion-fission process.

Our Flerov Laboratory of Nuclear Reactions (FLNR) theoretical group recently developed a calculation model that can treat all reaction processes in heavy- and superheavy-mass regions, the so-called unified model, which was applied to several types of reactions [12–14]. The unified model implies a unified dynamical approach and unified multidimensional potential energy. We take into account the time evolution from the diabatic potential to the adiabatic potential [15]. We connect the diabatic potential and adiabatic potential with a weight function on the relaxation time τ. We then perform a trajectory calculation on the time-dependent unified potential energy surface using the Langevin equation.

Here, we mainly analyze the experimental data obtained for the mass distribution of fission fragments (MDFF) in the reactions $^{36}S + ^{238}U$ and $^{30}Si + ^{238}U$ at several incident energies, which were measured by the Japan Atomic Energy Agency (JAEA) group [16,17]. The analysis of the MDFF is a powerful tool for investigating the mechanism of the reaction in the heavy-mass and superheavy-mass regions. These experimental data are very important because these reactions are in the intermediate region between the reactions $^{48}Ca + ^{208}Pb$ and $^{48}Ca + ^{238}U$; in the former reaction mass-symmetric fission events are dominant, while in the latter reaction mass-asymmetric fission events are dominant [9]. In the reaction $^{36}S + ^{238}U$, we can see that the ratio of Pb fragments to mass-symmetric fission fragments decreases with increasing incident energy. The shell-correction energy actually depends on the excitation energy or nuclear temperature, which disappears at high temperature. However, at the incident energy of $E_{c.m.} = 166.0$ MeV (corresponding to the excitation energy of the compound nucleus $E^* = 51.5$ MeV), a large number of Pb fragments can still be measured. This is evidence that the shell structure remains at such an excitation energy.

Using the dynamical model, we precisely investigate the incident energy dependence of MDFF. This study is the first

attempt to treat such experimental data systematically. We also consider the fine structures in the MDFF caused by the shell structure at a low incident energy. In the reaction $^{30}\mathrm{Si} + ^{238}\mathrm{U}$, there are two peaks at approximately $A = 90$ and 178 at a low incident energy, which do not correspond to nuclei with a closed shell. Using our model, we analyze the data obtained from this reaction in an attempt to understand the origin of these peaks.

The MDFF obtained from the experimental data includes contributions originating from the FF process and the QF process. We calculate the capture cross section σ_{cap} and the fusion cross section σ_{fus} and compare them with the experimental data. Experimentally, the fusion cross section is derived from counting the mass-symmetric fission events [9], which we here call the mass-symmetric fission cross section $\sigma_{A/2\pm20}$. In the theoretical calculation, however, sometimes σ_{fus} is 1 or 2 orders of magnitude smaller than $\sigma_{A/2\pm20}$ in the superheavy-mass region. The discrepancy between the experimentally and theoretically estimated values is discussed very often, but the problem has not been solved yet. In this study, we attempt to clarify the discrepancy.

In Sec. II, we briefly explain our framework in this study and the model. We show the calculation results of the MDFF in the reactions $^{36}\mathrm{S} + ^{236}\mathrm{U}$ and $^{30}\mathrm{Si} + ^{236}\mathrm{U}$ at several incident energies in Sec. III. In Sec. IV, we discuss the reason why the shape of the MDFF for both reactions are different from each other at the low incident energy. The general features and fine structures of the MDFF are investigated by analyzing the landscape of the potential energy surface and the behaviors of the trajectories. The results in the reaction $^{31}\mathrm{P} + ^{236}\mathrm{U}$ are presented in Sec. V. In Sec. VI, we present a summary of this study and further discussion.

II. MODEL

Mainly, we focus our attention on the dynamics of the FF process in the superheavy-mass region. In the experimental data for the mass and TKE distribution of fission fragments, each reaction type (FF process, QF process, DIC, elastic scattering, etc.) appears simultaneously and the reactions are coupled with each other. Therefore, we apply a unified dynamical approach and unified multidimensional potential energy, which were proposed by Zagrebaev and Greiner [12,13]. We perform a trajectory calculation on the potential energy surface. Thus, the whole evolution of the heavy nuclear system can be traced starting from the infinite distance between the projectile and target to the end of each process.

We apply a new method for the calculation of the multidimensional potential energy using the extended two-center shell model [15]. We take into account the time evolution from the diabatic potential $V_{\mathrm{diab}}(q)$ to the adiabatic potential $V_{\mathrm{adiab}}(q)$, here q denotes the collective coordinates of nuclear deformation. The diabatic potential is calculated by the folding procedure with an effective nucleon-nucleon interaction [12,13,15]. As shown in Fig. 4 in Ref. [12], we can see the "potential wall" in the overlap region of the colliding system. We use the adiabatic potential energy of the nuclear system calculated using the two-center shell model. We connect the diabatic potential and adiabatic potential with a weight function as follows:

$$\begin{aligned} V &= V_{\mathrm{diab}}(q) f(t) + V_{\mathrm{adiab}}(q)[1 - f(t)], \\ f(t) &= \exp\left(-\frac{t}{\tau}\right). \end{aligned} \tag{1}$$

Here, t is the time of interaction and $f(t)$ is a weight function on the relaxation time τ. We use the relaxation time $\tau = 10^{-21}$ sec, which was suggested in Ref. [18].

As the coordinates of nuclear deformation, we use the two-center parametrization [19,20] and employ three parameters as follows: z_0 (distance between two potential centers), δ (deformation of fragments), and α (mass asymmetry of the colliding nuclei); $\alpha = (A_1 - A_2)/(A_1 + A_2)$, where A_1 and A_2 denote the mass numbers of the target and the projectile, respectively [21]. The parameter δ is defined as $\delta = 3(a - b)/(2a + b)$, where a and b denote the half-length of the axes of the ellipse in the z_0 and ρ direction, respectively, as expressed in Fig. 1 in Ref. [19]. We assume that each fragment has the same deformations as the first approximation. δ is related to the deformation parameter β_2, which is familiar to us as

$$\beta_2 = \frac{\delta}{\sqrt{\frac{5}{16\pi}}(3 - \delta)}, \tag{2}$$

here $\delta < 1.5$ because of $a > 0$ and $b > 0$. To save computational time we use scaling and employ the coordinate z. The coordinate z is defined as $z = z_0/(R_{\mathrm{CN}} B)$, where R_{CN} denotes the radius of the spherical compound nucleus. The parameter B is defined as $B = (3 + \delta)/(3 - 2\delta)$.

In the two-center parametrization, the neck parameter is denoted by ϵ and is different in the entrance and exit channels [15]. Therefore, we employ $\epsilon = 1$ for the entrance channel and $\epsilon = 0.35$ for the exit channel to describe a realistic nuclear shape. We introduce the time-dependent potential energy surface in terms of ϵ using the relaxation time for ϵ of $\tau_\epsilon = 10^{-20}$ sec [22], as follows:

$$\begin{aligned} V_{\mathrm{adiab}} &= V_{\mathrm{adiab}}(q, \epsilon = 1) f_\epsilon(t) \\ &\quad + V_{\mathrm{adiab}}(q, \epsilon = 0.35)[1 - f_\epsilon(t)], \\ f_\epsilon(t) &= \exp\left(-\frac{t}{\tau_\epsilon}\right). \end{aligned} \tag{3}$$

We then perform the trajectory calculation on the time-dependent unified potential energy using the Langevin-type equation [12,13,21].

The nucleon transfer for slightly separated nuclei is somewhat possible. Such an intermediate nucleon exchange plays an important role in the fusion process at the incident energy near and below the Coulomb barrier. Before both nuclei come in contact, we treat the nucleon transfer using the producer described in Refs. [12,13] as

$$\frac{d\alpha}{dt} = \frac{2}{A_{\mathrm{CN}}} D_A^{(1)}(\alpha) + \frac{2}{A_{\mathrm{CN}}} \sqrt{D_A^{(2)}(\alpha) \Gamma_\alpha(t)}, \tag{4}$$

where the detail is explained in Refs. [12,13].

After the window of the touching nuclei opens sufficiently (hereafter "the mononucleus state"), the treatment of the evolution of the mass-asymmetric parameter α switches from the use of Eq. (4) to the use of the Langevin equation

with the procedure described in Ref. [21]. Therefore, the multidimensional Langevin equation [12,21] is given as

$$
\begin{aligned}
\frac{dq_i}{dt} &= (m^{-1})_{ij}p_j, \quad \frac{d\theta}{dt} = \frac{\ell}{\mu_R R^2},\\
\frac{d\varphi_1}{dt} &= \frac{L_1}{\Im_1}, \quad \frac{d\varphi_2}{dt} = \frac{L_2}{\Im_2},\\
\frac{dp_i}{dt} &= -\frac{\partial V}{\partial q_i} - \frac{1}{2}\frac{\partial}{\partial q_i}(m^{-1})_{jk}p_j p_k - \gamma_{ij}(m^{-1})_{jk}p_k\\
&\quad + g_{ij}R_j(t),\\
\frac{d\ell}{dt} &= -\frac{\partial V}{\partial \theta} - \gamma_{\rm tang}\left(\frac{\ell}{\mu_R R} - \frac{L_1}{\Im_1}a_1 - \frac{L_2}{\Im_2}a_2\right)R\\
&\quad + R g_{\rm tang}R_{\rm tang}(t),\\
\frac{dL_1}{dt} &= -\frac{\partial V}{\partial \varphi_1} + \gamma_{\rm tang}\left(\frac{\ell}{\mu_R R} - \frac{L_1}{\Im_1}a_1 - \frac{L_2}{\Im_2}a_2\right)a_1\\
&\quad - a_1 g_{\rm tang}R_{\rm tang}(t),\\
\frac{dL_2}{dt} &= -\frac{\partial V}{\partial \varphi_2} + \gamma_{\rm tang}\left(\frac{\ell}{\mu_R R} - \frac{L_1}{\Im_1}a_1 - \frac{L_2}{\Im_2}a_2\right)a_2\\
&\quad - a_2 g_{\rm tang}R_{\rm tang}(t),
\end{aligned}
\tag{5}
$$

where a summation over repeated indices is assumed. For the separated nuclei, q_i denotes the deformation coordinate specified by z and δ and to treat the evolution of α we use Eq. (4). For the mononucleus, q_i denotes the coordinate specified by z, δ, and α, and we do not use Eq. (4) for α. p_i is the conjugate momentum of q_i. V is the potential energy.

θ and ℓ are the relative orientation of nuclei and relative angular momentum, respectively. φ_1 and φ_2 are the angles of rotation of the nuclei in the reaction plane (their momentums of inertia and angular momentums are $\Im_{1,2}$ and $L_{1,2}$, respectively), $a_{1,2} = R/2 \pm (R_1 - R_2)/2$ are the distances from the centers of the fragments up to the middle point between nuclear surfaces, and $R_{1,2}$ are the nuclear radii. R is the distance between the nuclear centers (see Fig. 8 in Ref. [12]). The total angular momentum $L = \ell + L_1 + L_2$ is conserved. μ_R denotes the reduced mass. $\gamma_{\rm tang}$ is the friction force in the tangential direction of colliding nuclei. We are interested mainly in the reaction at near-barrier energies. The rotation of heavy nuclei is rather slow and orientation effects are remarkable. The orientation effects are affected by the initial orientations of statically deformed nuclei. Therefore, in Refs. [12,13], Eq. (4) was solved numerically assuming $\frac{\partial V}{\partial \varphi_1} = \frac{\partial V}{\partial \varphi_2} = 0$. However, in this study we assume the nose-to-nose collision as a first approximation. We restrict ourselves to a nose-to-nose geometry of the colliding nuclei, that is, we take the line connecting the centers of mass of the two colliding nuclei as the common symmetry axis for their deformation.

m_{ij} and γ_{ij} are the shape-dependent collective inertia parameter and friction tensor, respectively. For separated nuclei, we use the reduced mass and the phenomenological friction forces with the Woods-Saxon radial form factor, which is described in Refs. [12,13]. We switch the phenomenological friction to the friction for mononucleus using the smoothed function [12,13]. For the mononucleus, the wall-and-window one-body dissipation is adopted for the friction tensor and a hydrodynamical inertia tensor is adopted in the Werner-Wheeler approximation for the velocity field [23–25]. The normalized random force $R_i(t)$ is assumed to be white noise, that is, $\langle R_i(t)\rangle = 0$ and $\langle R_i(t_1)R_j(t_2)\rangle = 2\delta_{ij}\delta(t_1 - t_2)$. The strength of random force g_{ij} is given by $\gamma_{ij}T = \sum_k g_{ij}g_{jk}$, where T is the temperature of the compound nucleus calculated from the intrinsic energy of the composite system.

The adiabatic potential energy is defined as

$$V_{\rm adiab}(q, L, T) = V_{\rm LD}(q) + \frac{\hbar^2 L(L+1)}{2I(q)} + V_{\rm SH}(q, T), \tag{6}$$

$$V_{\rm LD}(q) = E_{\rm S}(q) + E_{\rm C}(q), \tag{7}$$

$$V_{\rm SH}(q, T) = E^0_{\rm shell}(q)\Phi(T), \tag{8}$$

$$\Phi(T) = \exp\left(-\frac{E^*}{E_{\rm d}}\right), \tag{9}$$

where $I(q)$ is the moment of inertia of a rigid body at deformation q. $V_{\rm LD}$ and $V_{\rm SH}$ are the potential energy of the finite-range liquid drop model and the shell-correction energy taking into account the temperature dependence. $E^0_{\rm shell}$ is the shell correction energy at $T = 0$. The temperature dependent factor $\Phi(T)$ is discussed in Ref. [26], where E^* denotes the excitation energy of the compound nucleus. The shell damping energy $E_{\rm d}$ is chosen as 20 MeV, which is given by Ignatyuk *et al.* [27].

$E_{\rm S}$ and $E_{\rm C}$ denote a generalized surface energy [28] and Coulomb energy, respectively. The centrifugal energy arising from the angular momentum L of the rigid body is also considered. The detail is explained in Ref. [21]. The intrinsic energy of the composite system $E_{\rm int}$ is calculated for each trajectory as

$$E_{\rm int} = E^* - \tfrac{1}{2}(m^{-1})_{ij}p_i p_j - V(q, L, T). \tag{10}$$

E^* is given by $E^* = E_{\rm c.m.} - Q$, where Q and $E_{\rm c.m.}$ denote the Q-value of the reaction and the incident energy in the center-of-mass frame, respectively. Each trajectory starts from a sufficiently large distance between both nuclei.

The capture and fusion cross sections are calculated as follows:

$$\sigma_{\rm cap} = \frac{\pi\hbar^2}{2\mu_0 E_{\rm c.m.}}\sum_{\ell=0}^{\infty}(2\ell+1)T_\ell(E_{\rm c.m.}, \ell), \tag{11}$$

$$\sigma_{\rm fus} = \frac{\pi\hbar^2}{2\mu_0 E_{\rm c.m.}}\sum_{\ell=0}^{\infty}(2\ell+1)P_{\rm CN}(E_{\rm c.m.}, \ell), \tag{12}$$

where μ_0 denotes the reduced mass in the entrance channel. $T_\ell(E_{\rm c.m.}, \ell)$ is the capture probability of the ℓth partial wave. $P_{\rm CN}(E_{\rm c.m.}, \ell)$ is the probability of forming a compound nuclei in competition with QF events. The method used to estimate the probabilities $T_\ell(E_{\rm c.m.}, \ell)$ and $P_{\rm CN}(E_{\rm c.m.}, \ell)$ by a dynamical calculation is explained in the next section.

III. INCIDENT ENERGY DEPENDENCE OF MASS DISTRIBUTION OF FISSION FRAGMENTS

A. Reaction of ^{36}S + ^{238}U

The fragment mass distributions for fission after a full momentum transfer were measured by the JAEA group for the

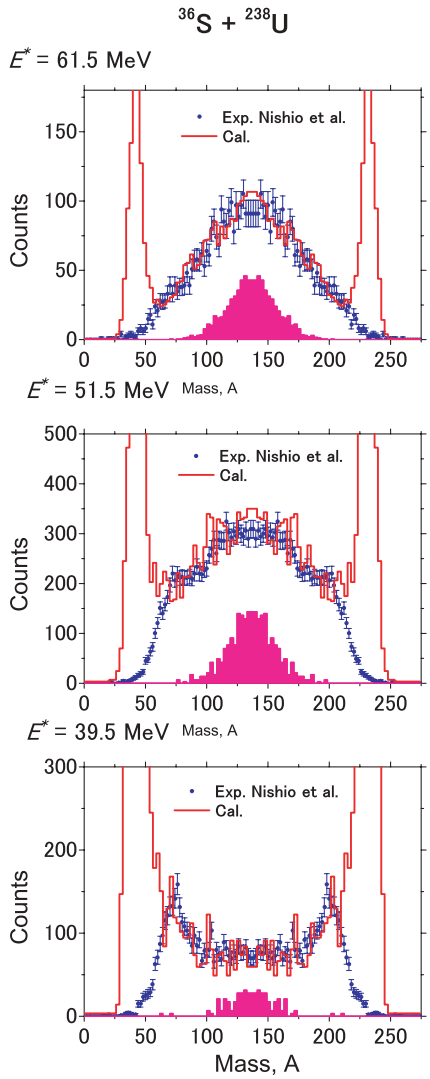

FIG. 1. (Color online) Mass distributions of fission fragments in the reaction $^{36}S + ^{238}U$. Experimental data and calculation results are denoted by circles [16] and histograms, respectively. Fusion-fission events correspond to shaded areas.

reaction $^{36}S + ^{238}U$ at several bombardment energies around the Coulomb barrier [16]. Figure 1 shows the MDFF at $E_{c.m.} = 176.0$ ($E^* = 61.5$) MeV, $E_{c.m.} = 166.0$ ($E^* = 51.5$) MeV, and $E_{c.m.} = 154.0$ ($E^* = 39.5$) MeV, which are denoted by circles. At the high incident energy, the mass-symmetric fission fragments are dominant. Nevertheless, at the low incident energy, the mass-asymmetric fission fragments are dominant. We can observe Pb fragments, which have a strong nuclear structure.

Since the nuclei of the actinides are prolately deformed, the Coulomb barrier height depends on the orientation of the target nuclei and reactions start from different configurations with the nuclei in contact. The two extreme cases are collisions at the poles and equator of the target nucleus. At a low projectile energy, nuclear contact only occurs in polar collisions, whereas at a higher energy, nuclear contact also occurs in equatorial collisions [10,11].

As a first approximation, we start the calculation for the spherical-spherical configuration at the high incident energy. Since all configurations are possible at the high incident energy, we use this assumption when considering average configurations. At the low incident energy, we take the initial condition as a collision with the pole of the target ^{238}U nucleus, whose deformation is $\beta_2 = 0.215$ ($\delta \sim 0.2$) [29]. Actually, it is difficult to calculate the adiabatic potential energy for subsequent shapes of a nuclear system starting from the configuration of two touching deformed nuclei with arbitrary orientation and up to nearly spherical compound nuclei.

The calculation results are denoted by histograms in Fig. 1. At the incident energies $E^* = 61.5$ MeV and $E^* = 51.5$ MeV, we start the calculation for the spherical-spherical configuration. With the low incident energy, $E^* = 39.5$ MeV, as the initial condition we consider the polar collision of the target. We use the relaxation times $\tau = 10^{-21}$ sec and $\tau_\epsilon = 10^{-20}$ sec, which are mentioned earlier. The temperature dependence of the shell-correction energy is taken into account. The calculations are normalized to agree with the experimental data in the mass-symmetric fission region. The trend of the experimental data, that is, the incident energy dependence of the MDFF, is reproduced by the calculation. However, there is a discrepancy for the very asymmetric mass region (above around $A = 210$ and below 40 or 50).

The MDFF in the experimental data includes only fission events and does not include the elastic and/or nucleon-transfer events, or deep inelastic components. In the experiment, fission events can be separated clearly from the elastic and/or nucleons transfer events as we can see in Fig. 1(c) of Ref. [16]. The mass distribution was obtained by using events entering in the "fission"-gate in Fig. 1(c). In addition, the fission events followed by the nucleon-transfer were removed in the off-line analysis by using the information on the fragment emission angle. That is, the experimental spectra include fission events when the momentum of the projectile is fully transferred to the system. However, the calculation was included in all processes. Therefore, the calculation results do not agree with the experimental data at a very asymmetric mass region.

The calculation and experimental data at the low incident energy show the peak around $A = 200$ in the MDFF. It seems that this peak originated from the shell effects, as *R.* Kalpakchieva *et al.* pointed out [30]. We precisely discuss the mechanism creating this peak in Sec. IV B.

Contrary to this idea, Kratz *et al.* explained this peak using another reason [31]. They carried out the experiment using a radiochemical procedure. In this case, products may be accumulated near the $A = 200$ region as α-decaying descendants of the nuclei around ^{238}U, produced by nuclear transfer reactions. However, the experimental data by Nishio were obtained by the in-beam experiment using detectors [16]. In this case, such decaying products cannot enter in the spectrum.

In the experiment, the cross sections for the full momentum transfer fission (σ_{fiss}) are shown in Fig. 2 as a function of the incident energy [16]. The cross sections are almost equal to those of the projectiles captured inside the Coulomb barrier. The calculation results for the capture cross section σ_{cap}

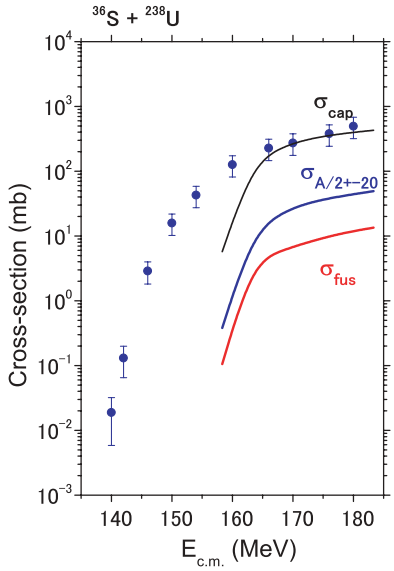

FIG. 2. (Color online) Excitation function of $\sigma_{\rm cap}$, $\sigma_{A/2\pm20}$, and $\sigma_{\rm fus}$ in the reaction $^{36}\mathrm{S} + ^{238}\mathrm{U}$. Experimental data of $\sigma_{\rm fiss}$ are denoted by circles [16].

and fusion cross section $\sigma_{\rm fus}$ are denoted by black and red lines, respectively. To estimate the cross sections, we start the calculation for the spherical-spherical configuration as a first approximation. The calculation using the Langevin equation is a classic one, therefore, we obtain the cross sections above the Bass barrier region ($V_{\rm c.m.}^{\rm Bass} = 158.8$ MeV) [32]. We calculate the capture cross section using the procedure in Refs. [9,33], in which the capture cross sections were derived by counting the events within a frame using a two-dimensional matrix of counts as a function of the mass and TKE. The calculated fusion cross section $\sigma_{\rm fus}$ is derived from the trajectory crossing the fusion region. We define the fusion region as the inside of the fission barrier in the three-dimensional coordinate space [21]. The blue line in Fig. 2 denotes the cross section $\sigma_{A/2\pm20}$, which derives from the yield of mass-symmetric fission fragments whose mass number is greater than $A_{\rm CN}/2 - 20$ and less than $A_{\rm CN}/2 + 20$, respectively. Here, $A_{\rm CN}$ denotes the mass number of the compound nucleus. The fusion cross section $\sigma_{\rm fus}$ is 1 or 2 orders of magnitude smaller than the cross section $\sigma_{A/2\pm20}$. In the MDFF, we also plot the fusion events, which are denoted by the shaded areas in Fig. 1. We can see that it is possible to obtain the mass-symmetric fission events in the QF process [21].

B. Reaction of ^{30}Si + ^{238}U

In the MDFF for the reaction $^{36}\mathrm{S} + ^{238}\mathrm{U}$ at the low incident energy, mass-asymmetric fission events are dominant. We can observe a peak near Pb fragments in Fig. 1. However, in the reaction $^{30}\mathrm{Si} + ^{238}\mathrm{U}$ at the low incident energy, the overall tendency and shape of the MDFF are different from those in the reaction $^{36}\mathrm{S} + ^{238}\mathrm{U}$. The MDFF in the reaction $^{30}\mathrm{Si} + ^{238}\mathrm{U}$ was also measured by the JAEA group [17]. In Fig. 3, the experimental data at the incident energies $E_{\rm c.m.} =$

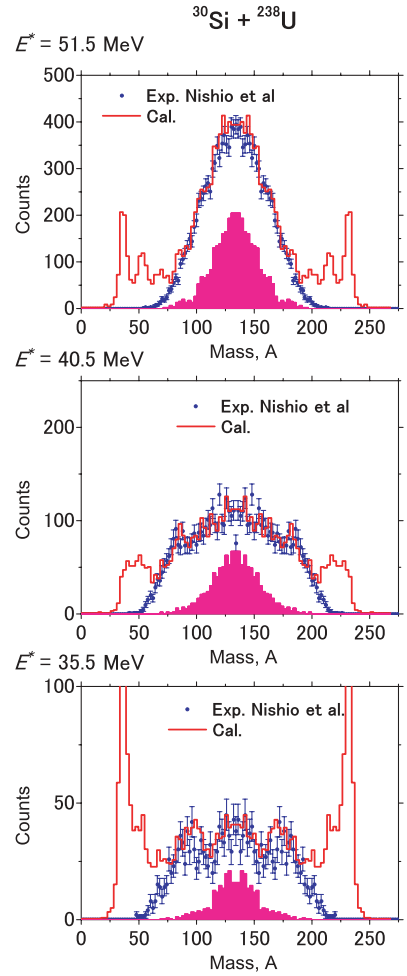

FIG. 3. (Color online) Mass distributions of fission fragments in the reaction $^{30}\mathrm{Si} + ^{238}\mathrm{U}$. Experimental data and calculation results are denoted by circles [17] and histograms, respectively. Fusion-fission events correspond to shaded areas.

144.0 ($E^* = 50.5$) MeV, $E_{\rm c.m.} = 134.0$ ($E^* = 40.5$) MeV, and $E_{\rm c.m.} = 129.0$ ($E^* = 35.5$) MeV are denoted by circles. At the low incident energy, $E^* = 35.5$ MeV, mass-symmetric fission events are dominant and three significant peaks appear at $A \sim 90, 134$, and 178. It is not obvious that the peaks at $A \sim 90$ and 178 correspond to nuclei with a strong nuclear structure.

The calculation results are shown in Fig. 3 as histograms, in which we use the same parameters as those in the reaction $^{36}\mathrm{S} + ^{238}\mathrm{U}$. At the incident energies, $E^* = 51.5$ MeV and $E^* = 40.5$ MeV, we start the calculation for the spherical-spherical configuration. At the low incident energy, $E^* =$ 35.5 MeV, we take the initial condition as a collision with the pole of the target ^{238}U nucleus. The results at high and low incident energies are in agreement with the tendencies of the experimental data. The calculation results of the capture cross section $\sigma_{\rm cap}$, fusion cross section $\sigma_{\rm fus}$, and mass symmetric fission cross section $\sigma_{A/2\pm20}$ are denoted by black, red, and blue lines in Fig. 4, respectively. We obtain these cross sections performing the calculation for the

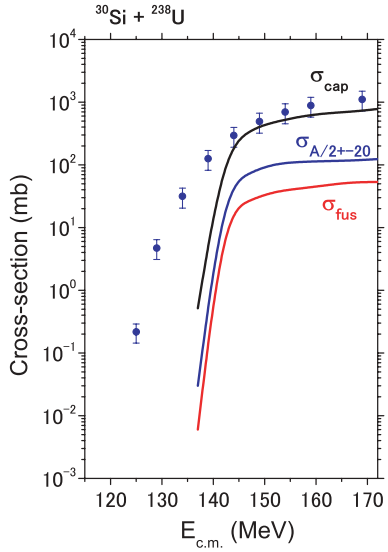

FIG. 4. (Color online) Excitation function of $\sigma_{\rm cap}$, $\sigma_{A/2\pm20}$, and $\sigma_{\rm fus}$ in the reaction ^{30}Si + ^{238}U. Experimental data of $\sigma_{\rm fiss}$ are denoted by circles [17].

spherical-spherical configuration as a first approximation. The Bass barrier of this system is $V_{\rm c.m.}^{\rm Bass} = 141.1$ MeV. $\sigma_{\rm fus}$ is 1 or 2 orders of magnitude smaller than the cross section $\sigma_{A/2\pm20}$, which shows the same tendency as that in the reaction ^{36}S + ^{238}U. We also plot the fusion events, which are denoted by the shaded area in Fig. 3. It shows that mass-symmetric fission events come from both the FF process and QF process.

IV. ANALYSIS OF MASS DISTRIBUTION OF FISSION FRAGMENTS AT LOW INCIDENT ENERGY

A. General features of mass distribution of fission fragments

The most interesting challenge is to understand the reason why the shapes of the MDFF for the reactions ^{36}S + ^{238}U and ^{30}Si + ^{238}U are different from each other at the low incident energy. The compound nuclei produced in each reaction (Z = 108 and 106) are intermediate systems between those produced in the reactions ^{48}Ca + ^{208}Pb and ^{48}Ca + ^{238}U (Z numbers of the compound nuclei are Z = 102 and 112, respectively); in the former, mass-symmetric fission events are dominant and in the latter, mass-asymmetric fission events are dominant, which were measured by the FLNR group [9]. Thus, the reactions ^{36}S + ^{238}U and ^{30}Si + ^{238}U may correspond to transitional systems from mass-symmetric fission to mass-asymmetric fission.

In the reaction ^{30}Si + ^{238}U at a low incident energy, we attempt to clarify the origin of the peaks at $A \sim 90$, 134, and 178 in the MDFF. The MDFF is essentially governed by the dynamics of the trajectory in the potential energy surface and it is affected by the inertia mass, the friction, and the relaxation times τ and τ_ϵ. Though the MDFF is under the influence of many factors, we try to find the main contributor to control the fine structure and the general feature of the MDFF. The shape of the MDFF is affected by the landscape of the potential energy surface because the trajectories are affected by the potential energy surface. The potential energy surface depends on the temperature owing to the temperature dependence of the shell-correction energy.

We first attempt to determine the effect of the potential energy surface by calculating the MDFF using the potential energy in the liquid drop model for the adiabatic potential energy part and that with the full shell-correction energy, which corresponds to the potential energy surface at T = 0 MeV. These potential energies are represented by $V_{\rm LD}$ and $V_{\rm LD} + E^0_{\rm shell}$, respectively. The results for $V_{\rm LD}$ and $V_{\rm LD} + E^0_{\rm shell}$ in the reaction ^{36}S + ^{238}U at $E^* = 39.5$ MeV are shown in Figs. 5(a) and 5(b), respectively. The experimental data are denoted by circles [16]. When we employ the potential energy $V_{\rm LD}$, the general shape of the MDFF is convex as shown in Fig. 5(a). Although the calculated MDFF does not reproduce the peak due to Pb fragments, it represents the general trend of the experimental data. Furthermore, when we use $V_{\rm LD} + E^0_{\rm shell}$, peaks appear at $A \sim 80$ and 180 as shown in Fig. 5(b) and the overall trend does not correspond to the experimental data.

We perform the same calculation for the reaction ^{30}Si + ^{238}U at $E^* = 35.5$ MeV, and the results for $V_{\rm LD}$ and $V_{\rm LD} + E^0_{\rm shell}$ are shown in Figs. 6(a) and 6(b), respectively. In this reaction, when we use $V_{\rm LD}$, the calculated MDFF has a concave shape and corresponds to the general trend of the experimental data. When we use $V_{\rm LD} + E^0_{\rm shell}$, we can observe two peaks at $A \sim 90$ and 175, similarly to those observed in the result for ^{36}S + ^{238}U using $V_{\rm LD} + E^0_{\rm shell}$. The positions of the two peaks agree with the experimental data. However, mass-asymmetric fission events do not appear and the general trend of the MDFF does not agree with the experimental data.

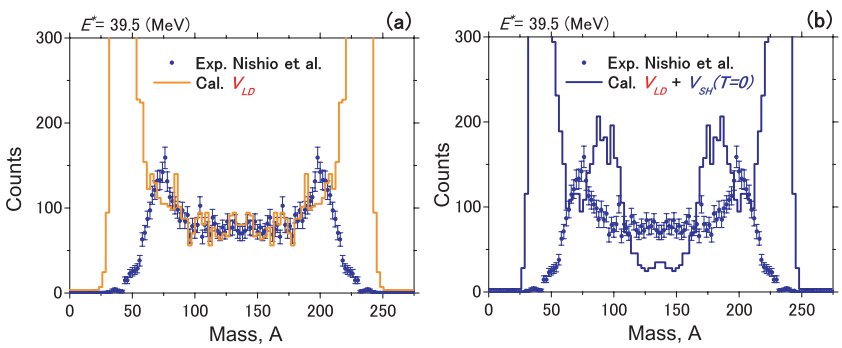

FIG. 5. (Color online) Mass distributions of fission fragments for $V_{\rm LD}$ (a) and $V_{\rm LD} + E^0_{\rm shell}$ (b) at $E^* = 39.5$ MeV in the reaction ^{36}S + ^{238}U. Experimental data are denoted by circles [16].

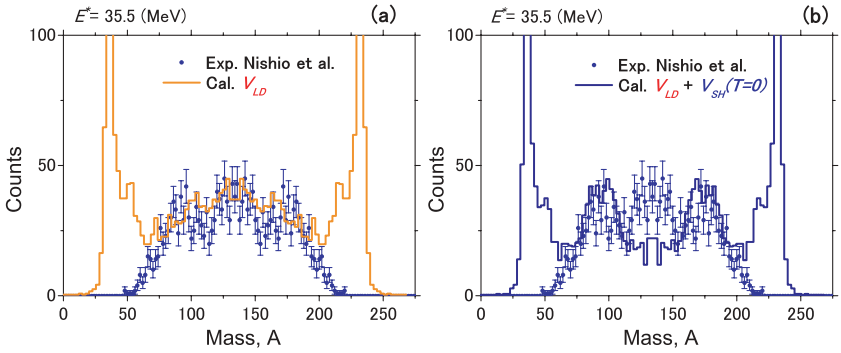

FIG. 6. (Color online) Mass distributions of fission fragments for $V_{\rm LD}$ (a) and $V_{\rm LD} + E^0_{\rm shell}$ (b) at $E^* = 35.5$ MeV in the reaction ^{30}Si + ^{238}U. Experimental data are denoted by circles [17].

B. Effect of the shell correction energy

We now discuss the landscape of the potential energy surface at the scission point, which is directly connected with the shape of the MDFF. Figures 7(a) and 7(b) show the adiabatic potential energy surface near the scission point of the nuclei ^{274}Hs and ^{268}Sg, which are produced in the reactions ^{36}S + ^{238}U and ^{30}Si + ^{238}U, respectively. $V_{\rm LD}$ and $V_{\rm LD} + E^0_{\rm shell}$ with $\delta = 0.22$ are denoted by red and blue lines, respectively. The numbers near the lines denote values of the deformation parameter δ. For $\delta = 0.16$, the yellow and light-blue lines denote $V_{\rm LD}$ and $V_{\rm LD} + E^0_{\rm shell}$, respectively. Although the trajectory of the FF process approaches the compact shape region and moves to the reseparation region with a large deformation, the trajectory of the QF process quickly moves to the reseparation region and usually does not have sufficient time for the fragments to markedly deform dynamically [26,34].

For the potential energy $V_{\rm LD} + E^0_{\rm shell}$ of both ^{274}Hs and ^{268}Sg, we can observe valleys at $A \sim 80$ and 180. Generally, owing to the nuclear structure, the shell-correction energy $E^0_{\rm shell}$ is large at $A \sim 208$, which corresponds to the nucleus ^{208}Pb. However, in the case of $V_{\rm LD} + E^0_{\rm shell}$, as shown in Fig. 7, because $V_{\rm LD}$ has a parabolic shape, at the scission point the valley based on the shell-correction energy of ^{208}Pb shifts to a more mass-symmetric region. Thus, the valleys appear at $A \sim 80$ and 180. Therefore, when we use $V_{\rm LD} + E^0_{\rm shell}$, the peaks appear at $A \sim 80$ and 180 in the reaction ^{36}S + ^{238}U, and at $A \sim 90$ and 175 in the reaction ^{30}Si + ^{238}U in the MDFF. We consider this as a detailed feature of the MDFF.

C. Effect of diabatic potential energy surface

Next we consider the effect of the diabatic potential energy surface. In our model, at the early stage of the reaction process, the trajectories appear to be affected by the diabatic potential. The events in the mass-asymmetric fission part (around the injection point) of the MDFF mainly originate from the trajectories with short reaction times, such as elastic scattering, the DIC process, and the QF process with a small number of nucleons transferred. Therefore, these processes are affected by the diabatic potential energy surface.

Figures 8(a) and 8(b) show the diabatic potential energy surface at the contact point leading to the compound nuclei ^{274}Hs and ^{268}Sg, respectively. The numbers near the lines denote values of the deformation parameter δ.

We can see a strong fluctuating structure in the diabatic potential as a function of the mass asymmetry. It originates from the difference among the reaction Q-values for each combination leading to the same compound nucleus. We define the origin of the potential energy as the ground state of the compound nucleus with the liquid drop model, which is obtained by the reaction ^{36}S + ^{238}U in Fig. 8(a) and ^{30}Si + ^{238}U in Fig. 8(b), respectively. We apply these origins for another combination leading to the same compound nucleus.

For $\delta = 0$, we can observe a valley at approximately $A \sim 208$, which corresponds to ^{208}Pb in Fig. 8(a), but in Fig. 8(b) the valley at $A \sim 208$ is not pronounced. This valley corresponds to the so-called cold fusion valley [35,36]. When we take into account the deformation of the target nuclei, the valley is not particulary remarkable.

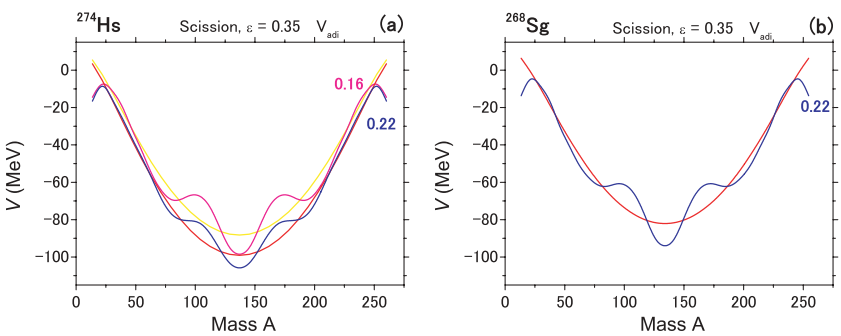

FIG. 7. (Color online) Adiabatic potential energy surface near the scission point of the nuclei ^{274}Hs (a) and ^{268}Sg (b). $V_{\rm LD}$ and $V_{\rm LD} + E^0_{\rm shell}$ are denoted by red and blue lines, respectively. The numbers near the lines denote values of the deformation parameter δ.

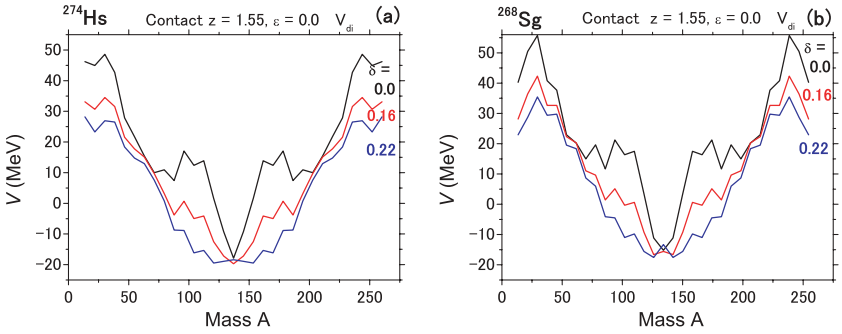

FIG. 8. (Color online) Diabatic potential energy surface at the contact point leading to the compound nuclei ^{274}Hs (a) and ^{268}Sg (b). The numbers near the lines denote values of the deformation parameter δ.

According to the analysis in the previous section, in the reaction $^{36}\mathrm{S} + ^{238}\mathrm{U}$ at the low incident energy, the QF process with a short reaction time is dominant because mass-asymmetric fission events are dominant. Therefore, the trajectories are mainly affected by the diabatic potential energy surface. Nevertheless, in the reaction $^{30}\mathrm{Si} + ^{238}\mathrm{U}$ at the low incident energy, since the QF process with a long reaction time, which we call the "deep quasifission process," [21] is dominant, the trajectories are mainly affected by the adiabatic potential energy surface.

D. Analysis of the reaction dynamics using sample trajectories

We next discuss the origin of the QF process with the long and short reaction time by analyzing sample trajectories. The trajectory analysis allows us to directly observe the time evolution of the dynamical process [34]. Figure 9 shows sample trajectories projected onto the z-V plane. That is to say, they correspond to the potential energy surface that the trajectories actually pass through. The trajectories in the reaction $^{36}\mathrm{S} + ^{238}\mathrm{U}$ at $E^* = 39.5$ MeV and in the reaction $^{30}\mathrm{Si} + ^{238}\mathrm{U}$ at $E^* = 35.5$ MeV with $\ell = 0$ are shown in Figs. 9(a) and 9(b), respectively. Each trajectory in Fig. 9(b) is calculated using the same initial random numbers as those for each trajectory in Fig. 9(a).

Although some of the trajectories in the reaction $^{30}\mathrm{Si} + ^{238}\mathrm{U}$ reach the compact shape region $z \sim 0$ after overcoming the Coulomb barrier, the trajectories in the reaction $^{36}\mathrm{S} + ^{238}\mathrm{U}$ return to the reseparation region even if they overcome the barrier. Figures 10(a) and 10(b) show the same trajectories, which are projected on the z-α and z-δ planes in the reaction $^{36}\mathrm{S} + ^{238}\mathrm{U}$, respectively. The arrows denote the injection points of those reactions. As shown in Fig. 10(a), the trajectories cannot enter the small-z region and do not have sufficient time to transfer the nucleons between the nuclei. Therefore, the trajectories move to the reseparation region without changing the α parameter significantly. In Fig. 10(b), after the trajectories overcome the Coulomb barrier and reach the wall of the diabatic potential, they proceed in the $+\delta$ direction. It appears that they move along the valley ($z \sim 1.2$, $0.2 < \delta < 0.7$), which follows the pockets of the diabatic potential energy surface.

Moreover, in the reaction $^{30}\mathrm{Si} + ^{238}\mathrm{U}$, since the trajectories can enter the small-z region, they have sufficient time to change the α parameter significantly, then some of them can exit the mass-symmetric fission region. The trajectories projected onto the z-α and z-δ planes are shown in Figs. 11(a) and 11(b), respectively. According to Fig. 11(a), trajectories exist that enter the reseparation region with $A \sim 175$ ($\alpha \sim 0.3$). In Fig. 11(b), although the trajectories follow the valley of the diabatic potential similarly to the trajectories in the reaction $^{36}\mathrm{S} + ^{238}\mathrm{U}$, some of them enter the small-z region. After overcoming the Coulomb barrier, such trajectories remain around the region of $z \sim 1.2$ for some time owing to their fluctuation and during that time the potential energy surface changes from a diabatic potential to an adiabatic potential. Then the trajectories can enter the small-z region owing to the disappearance of the wall of the diabatic potential. In the reaction $^{30}\mathrm{Si} + ^{238}\mathrm{U}$, it appears that the average time that the trajectories spend in the region around $z \sim 1.2$ is longer than that in the reaction $^{36}\mathrm{S} + ^{238}\mathrm{U}$. This is one of the reasons that the overall trend of the MDFF is different between the reactions $^{30}\mathrm{Si} + ^{238}\mathrm{U}$ and $^{36}\mathrm{S} + ^{238}\mathrm{U}$ at the low incident energy.

To analyze the characteristic behavior of sample trajectories in the reactions $^{36}\mathrm{S} + ^{238}\mathrm{U}$ and $^{30}\mathrm{Si} + ^{238}\mathrm{U}$, we employ the mean trajectory. In Fig. 12, the red and thin blue lines

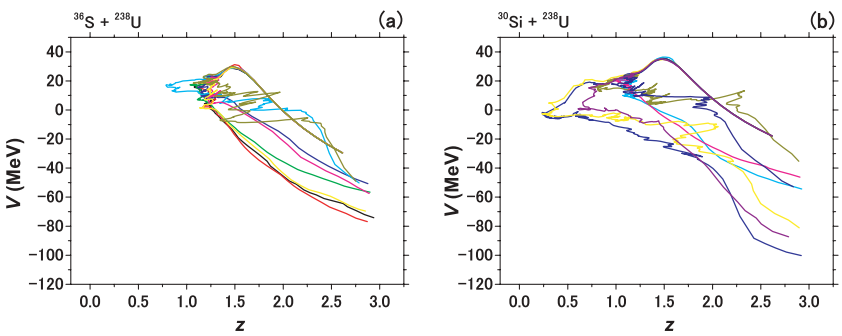

FIG. 9. (Color online) Sample trajectories projected onto the z-V plane in the reaction $^{36}\mathrm{S} + ^{238}\mathrm{U}$ at $E^* = 39.5$ MeV with $\ell = 0$ (a) and in the reaction $^{30}\mathrm{Si} + ^{238}\mathrm{U}$ at $E^* = 35.5$ MeV with $\ell = 0$ (b).

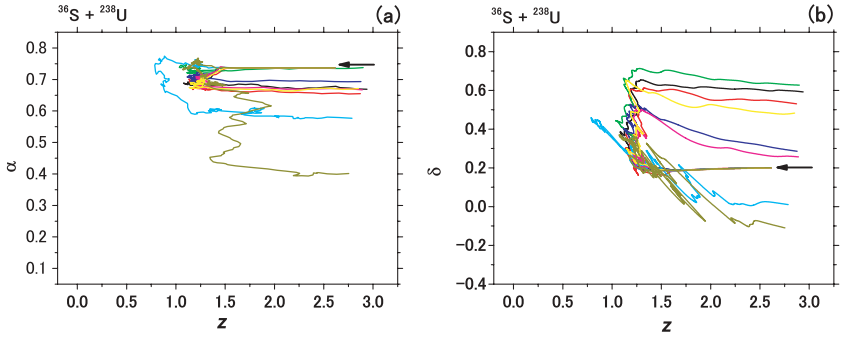

FIG. 10. (Color online) Sample trajectories projected on the z-α (a) and z-δ (b) planes in the reaction $^{36}\mathrm{S} + ^{238}\mathrm{U}$ at $E^* = 39.5$ MeV, respectively. The arrows denote the injection points of this reaction.

denote the mean trajectories in the reaction $^{36}\mathrm{S} + ^{238}\mathrm{U}$ at $E^* = 39.5$ MeV using V_{LD} and $V_{\mathrm{LD}} + E^0_{\mathrm{shell}}$ for the adiabatic potential energy part, respectively. The orange and thin light-blue lines denote the mean trajectories in the reaction $^{30}\mathrm{Si} + ^{238}\mathrm{U}$ at $E^* = 35.5$ MeV, using V_{LD} and $V_{\mathrm{LD}} + E^0_{\mathrm{shell}}$, respectively.

As discussed in the previous section, when we use V_{LD}, we can observe the overall trend of the MDFF. The mean trajectories collide with the wall of the diabatic potential at points A and B in Fig. 12 in the reactions $^{36}\mathrm{S} + ^{238}\mathrm{U}$ and $^{30}\mathrm{Si} + ^{238}\mathrm{U}$, respectively. Then the trajectories proceed in the $+\delta$ direction and finally move to the reseparation region. The value of z at position B is smaller than that at position A. This slight difference of the positions, which originates from the difference of the potential energy surface, appears to determine whether mass-symmetric fission events or mass-asymmetric fission events are dominant. Actually, when we use $V_{\mathrm{LD}} + E^0_{\mathrm{shell}}$, the mean trajectory in the reaction $^{30}\mathrm{Si} + ^{238}\mathrm{U}$ can enter the small-z region at B, although in the reaction $^{36}\mathrm{S} + ^{238}\mathrm{U}$ it cannot enter the small-z region, similar to the case when we use V_{LD}.

Figure 13 shows the diabatic potential energy with $\delta = 0.2$ and $\ell = 0$ in the reactions $^{36}\mathrm{S} + ^{238}\mathrm{U}$ and $^{30}\mathrm{Si} + ^{238}\mathrm{U}$, which are denoted by black and red lines, respectively. The position of the wall of the potential for the reaction $^{30}\mathrm{Si} + ^{238}\mathrm{U}$ is inside (i.e., at a position with a smaller value of z) that for the reaction $^{36}\mathrm{S} + ^{238}\mathrm{U}$. Therefore, the trajectory in the reaction $^{30}\mathrm{Si} + ^{238}\mathrm{U}$ collides with the wall at a smaller value of z than that in the reaction $^{36}\mathrm{S} + ^{238}\mathrm{U}$.

The general future of MDFF is affected by the landscape of potential energy around the contact point, which is created by the delicate balance between the diabatic potential and V_{LD} of the adiabatic potential.

V. MASS DISTRIBUTION OF FISSION FRAGMENTS IN REACTION $^{31}\mathrm{P} + ^{238}\mathrm{U}$

As discussed previously, the general futures of the MDFF for $^{36}\mathrm{S} + ^{238}\mathrm{U}$ and $^{30}\mathrm{Si} + ^{238}\mathrm{U}$ at the low excitation energy are clearly different; the MDFF has a concave shape and a convex shape, respectively. The former reaction leads to a compound nucleus with $Z = 108$ and the latter leads to one with $Z = 106$. Here, as an intermediate system between them, we consider the reaction $^{31}\mathrm{P} + ^{238}\mathrm{U}$, which leads to a compound nucleus with $Z = 107$, using the same values of the parameters as those in the previous section. The experiment in this reaction was done by the JAEA group in March 2009 and now they are analyzing the data. The calculation results of the MDFF are shown in Fig. 14 at the incident energies $E^* = 60$, 50, and 45 MeV. In this reaction, the Bass barrier in the excitation energy is rather high, $V^*_{\mathrm{Bass}} = 57.4$ MeV, compared with that for the reactions $^{36}\mathrm{S} + ^{238}\mathrm{U}$ ($V^*_{\mathrm{Bass}} = 45.5$ MeV) and $^{30}\mathrm{Si} + ^{238}\mathrm{U}$ ($V^*_{\mathrm{Bass}} = 51.3$ MeV) [32]. Therefore, at the incident energy $E^* = 60$ MeV, we start the calculation assuming the spherical-spherical configuration as an initial condition. At the incident energies, $E^* = 50$ and 45 MeV, as initial conditions, we consider the polar collision of the target.

In Fig. 14, the general trend at $E^* = 45$ MeV is similar to that in the reaction $^{30}\mathrm{Si} + ^{238}\mathrm{U}$. Moreover, we can observe peaks at $A \sim 100$ and 170, which are caused by the landscape of the adiabatic potential energy surface. Figure 15 shows the capture cross section σ_{cap}, the mass symmetric cross section $\sigma_{A/2\pm 20}$, and the fusion cross section σ_{fus}, which are denoted by black, blue, and red lines, respectively. We also plot the fusion events, which are denoted by the shaded areas in Fig. 14. The results show that mass-symmetric fission events originate not only from the FF process but also from the QF process.

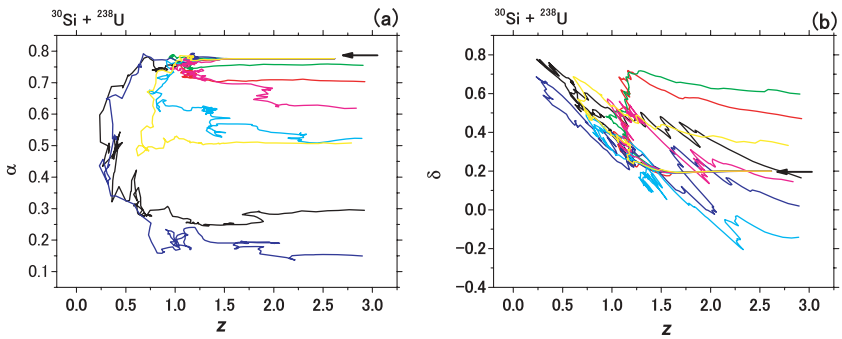

FIG. 11. (Color online) Sample trajectories projected on the z-α (a) and z-δ (b) planes in the reaction $^{30}\mathrm{Si} + ^{238}\mathrm{U}$ at $E^* = 35.5$ MeV, respectively. The arrows denote the injection points of this reaction.

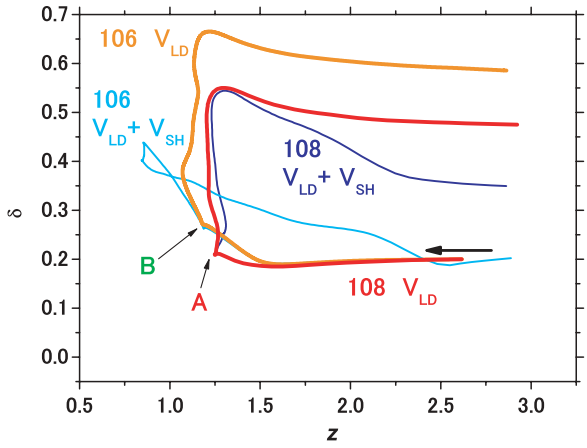

FIG. 12. (Color online) Mean trajectories in the reaction $^{36}S + ^{238}U$ at $E^* = 39.5$ MeV using the adiabatic potential energies V_{LD} and $V_{LD} + E^0_{shell}$ are denoted by red and thin blue lines, respectively. The orange and thin light-blue lines denote the mean trajectories in the reaction $^{30}Si + ^{238}U$ at $E^* = 35.5$ MeV, using the potential energies V_{LD} and $V_{LD} + E^0_{shell}$, respectively. *A* and *B* denote the position where the trajectories collide with the wall of the diabatic potential in the reactions $^{36}S + ^{238}U$ and $^{30}Si + ^{238}U$, respectively.

VI. SUMMARY

In this article we analyze the experimental data obtained for the MDFF in the reactions $^{36}S + ^{238}U$ and $^{30}Si + ^{238}U$ at several incident energies, which were measured by the JAEA group [16,17]. We apply a unified model and perform a trajectory calculation. The incident energy dependence of the MDFF is precisely investigated. This study is a first attempt to treat such experimental data systematically. We also discuss the fine structures in the MDFF caused by the shell structure at a low incident energy.

In the MDFF in the reaction $^{36}S + ^{238}U$, at the high incident energy, the mass-symmetric fission fragments are dominant. Furthermore, at the low incident energy, the mass-asymmetric fission fragments are dominant. The trend of the experimental data was reproduced by the calculation. At the low incident energy, it is significant that we take the initial condition as a collision with the pole of the target ^{238}U nucleus. We also stress that it is very important to consider the temperature dependence of shell-correction energy on the potential energy surface.

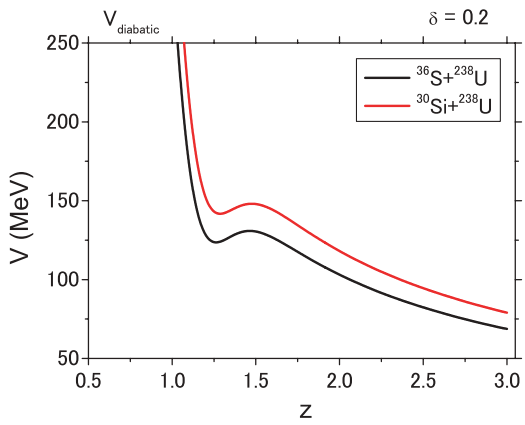

FIG. 13. (Color online) Diabatic potential energy with $\delta = 0.2$ and $\ell = 0$ in the reactions $^{36}S + ^{238}U$ and $^{30}Si + ^{238}U$ are denoted by black and red lines, respectively.

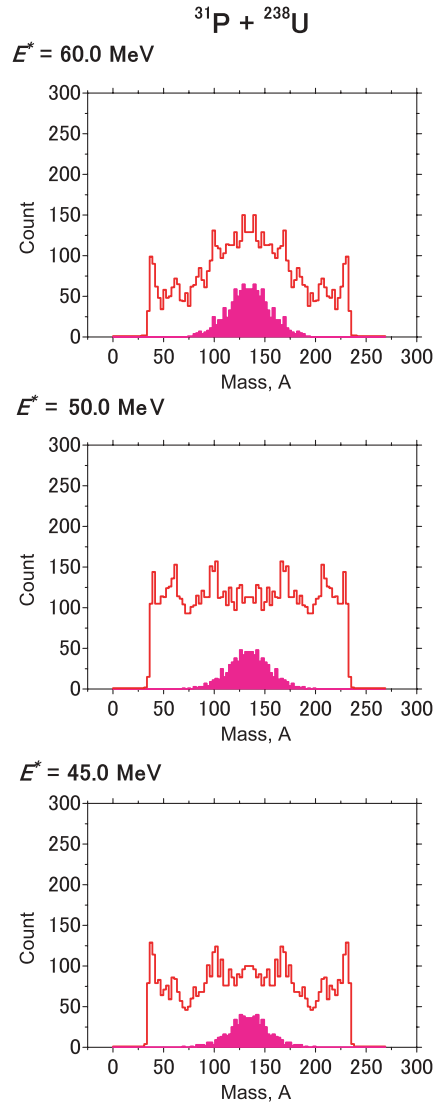

FIG. 14. (Color online) Calculated mass distributions of fission fragments in the reaction $^{31}P + ^{238}U$. Fusion-fission events correspond to shaded areas.

In the MDFF for the reaction $^{36}S + ^{238}U$ at the low incident energy, mass-asymmetric fission events are dominant. Nevertheless, in the reaction $^{30}Si + ^{238}U$, mass-symmetric fission events are dominant. Thus, the reactions $^{36}S + ^{238}U$ and $^{30}Si + ^{238}U$ correspond to transitional systems from mass-symmetric fission to mass-asymmetric fission, that is to say, the distribution changes from a convex shape to a concave shape.

We investigate the reason why the shapes of the MDFF for both reactions are different from each other at the low incident energy. The shape of the MDFF is affected by the landscape of the potential energy surface. Therefore, we investigate the effect of the potential energy surface by calculating the MDFF using the potential energy V_{LD} and $V_{LD} + E^0_{shell}$ for

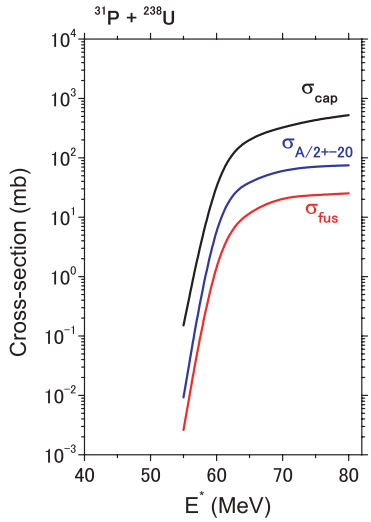

FIG. 15. (Color online) Excitation function of $\sigma_{\rm cap}$, $\sigma_{A/2\pm20}$, and $\sigma_{\rm fus}$ in the reaction ^{31}P + ^{238}U.

the adiabatic potential energy part. When we use $V_{\rm LD} + E^0_{\rm shell}$, the peaks appear at $A \sim 90$ and 178 in the reaction ^{30}Si + ^{238}U in the MDFF because the potential energy surface has valleys at $A \sim 90$ and 180 which appear owing to the balance between $V_{\rm LD}$ and $E^0_{\rm shell}$. This is a fine feature of the MDFF. Nevertheless, the general features of the MDFF appear to be mainly governed by the landscape of potential energy around the contact point, which is caused by the delicate balance between the diabatic potential and $V_{\rm LD}$ of the adiabatic potential. It determines whether the distribution has a convex or concave shape.

The trajectory analysis allows us to directly observe the time evolution of the dynamical process. The main reason for the difference between the general features of the MDFF in the reactions ^{36}S + ^{238}U and ^{30}Si + ^{238}U at the low incident energy is the slight difference between the positions at which the trajectories collide with the wall of the diabatic potential. This slight difference determines whether mass-symmetric fission or mass-asymmetric fission is dominant.

In the next step, we should consider all orientation effects of the colliding nuclei that play an important role in the sub-barrier fusion of deformed nuclei and estimate the capture cross section and fusion cross section. In the experiment, the evaporation residue cross section is measured at the sub-barrier region [16,17]. We precisely investigate the role of the orientation effects and the mechanism of the enhancement of the capture and fusion cross sections.

ACKNOWLEDGMENTS

The author is grateful to Prof. V. I. Zagrevaev, Prof. W. Greiner, Dr. A. V. Karpov, and Prof. F. Hanappe for their helpful suggestions and valuable discussion. Special thanks go to Dr. A. K. Nasirov, Dr. A. S. Denikin, and Prof. K. Hagino for their helpful comments, to Dr. K. Nishio, Dr. H. Ikezoe, and the JAEA experimental group for providing us with the experimental data and their helpful discussion. The diabatic potential and adiabatic potential were calculated using the NRV code [15]. The numerical calculations were carried out on SX8 at YITP in Kyoto University. This work was performed partially when the author stayed at Universite Libre de Bruxelles.

[1] W. D. Myers and W. J. Swiatecki, Nucl. Phys. **81**, 1 (1966); A. Sobiczewski, F. A. Gareev, and B. N. Kalinkin, Phys. Lett. **22**, 500 (1966).
[2] Yu. Ts. Oganessian *et al.*, Nature (London) **400**, 242 (1999); Phys. Rev. Lett. **83**, 3154 (1999); Phys. Rev. C **63**, 011301(R) (2000); **69**, 021601(R) (2004).
[3] S. Hofmann and G. Münzenberg, Rev. Mod. Phys. **72**, 733 (2000); S. Hofmann *et al.*, Eur. Phys. J. A **14**, 147 (2002).
[4] K. Morita *et al.*, J. Phys. Soc. Jpn. **73**, 2593 (2004); K. Morita *et al.*, *ibid.* **76**, 043201 (2007).
[5] K. Satou, H. Ikezoe, S. Mitsuoka, K. Nishio, and S. C. Jeong, Phys. Rev. C **65**, 054602 (2002).
[6] H. Ikezoe, K. Satou, S. Mitsuoka, K. Nishio, and S. C. Jeong, Phys. Atom. Nucl. **66**, 1053 (2003).
[7] P. Möller, J. R. Nix, P. Armbruster, S. Hofmann, and G. Münzenberg, Z. Phys. A **359**, 251 (1997).
[8] P. Armbruster, Rep. Prog. Phys. **62**, 465 (1999).
[9] M. G. Itkis *et al.*, Nucl. Phys. **A734**, 136 (2004); **A787**, 150c (2007).
[10] S. Mitsuoka, H. Ikezoe, K. Nishio, and J. Lu, Phys. Rev. C **62**, 054603 (2000).
[11] K. Nishio, H. Ikezoe, S. Mitsuoka, and J. Lu, Phys. Rev. C **62**, 014602 (2000); K. Nishio, H. Ikezoe, S. Mitsuoka, K. Satou, and S. C. Jeong, *ibid.* **63**, 044610 (2001).
[12] V. Zagrebaev and W. Greiner, J. Phys. G **31**, 825 (2005).
[13] V. Zagrebaev and W. Greiner, J. Phys. G **34**, 1 (2007); **34**, 2265 (2007).
[14] V. Zagrebaev and W. Greiner, Phys. Rev. Lett. **101**, 122701 (2008); Phys. Rev. C **78**, 034610 (2008); J. Phys. G **35**, 125103 (2008).
[15] V. I. Zagrebaev, A. V. Karpov, Y. Aritomo, M. A. Naumenko, and W. Greiner, Phys. Part. Nuclei **38**, 469 (2007); NRV codes for driving potential, http://nrv.jinr.ru/nrv/.
[16] K. Nishio, H. Ikezoe, S. Mitsuoka, I. Nishinaka, Y. Nagame, Y. Watanabe, T. Ohtsuki, K. Hirose, and S. Hofmann, Phys. Rev. C **77**, 064607 (2008).
[17] K. Nishio, H. Ikezoe, S. Mitsuoka, I. Nishinaka, Y. Watanabe, Y. Nagame, T. Ohtsuki, K. Hirose, and S. Hofmann (to be published).
[18] G. F. Bertsch, Z. Phys. A **289**, 103 (1978); W. Cassing and W. Nörenberg, Nucl. Phys. **A401**, 467 (1983); A. Diaz-Torres, Phys. Rev. C **69**, 021603(R) (2004).
[19] J. Maruhn and W. Greiner, Z. Phys. **251**, 431 (1972).
[20] K. Sato, A. Iwamoto, K. Harada, S. Yamaji, and S. Yoshida, Z. Phys. A **288**, 383 (1978).
[21] Y. Aritomo and M. Ohta, Nucl. Phys. **A744**, 3 (2004).
[22] A. Karpov (private communication).
[23] J. Blocki, Y. Boneh, J. R. Nix, J. Randrup, M. Robel, A. J. Sierk, and W. J. Swiatecki, Ann. Phys. (NY) **113**, 330 (1978).

[24] J. R. Nix and A. J. Sierk, Nucl. Phys. **A428**, 161c (1984).
[25] H. Feldmeier, Rep. Prog. Phys. **50**, 915 (1987).
[26] Y. Aritomo, Nucl. Phys. **A780**, 222 (2006).
[27] A. V. Ignatyuk, G. N. Smirenkin, and A. S. Tishin, Sov. J. Nucl. Phys. **21**, 255 (1975).
[28] H. J. Krappe, J. R. Nix, and A. J. Sierk, Phys. Rev. C **20**, 992 (1979).
[29] P. Möller, J. R. Nix, W. D. Myers, and W. J. Swiatecki, At. Data Nucl. Data Tables **59**, 185 (1995).
[30] R. Kalpakchieva, Yu. Ts. Oganessian, Yu. E. Penionzhkevich, and H. Sodan, Z. Phys. A **283**, 253 (1977).
[31] J. V. Kratz, A. E. Norris, and G. T. Seaborg, Phys. Rev. Lett. **33**, 502 (1974).
[32] R. Bass, Nucl. Phys. **A231**, 45 (1974); *Nuclear Reactions with Heavy Ions* (Springer, Berlin, 1980).
[33] W. Q. Shen, J. Albinski, A. Gobbi, S. Gralla, K. D. Hildenbrand, N. Herrmann, J. Kuzminski, W. F. J. Muller, H. Stelzer, J. Toke, B. B. Back, S. Bjornholm, and S. P. Sorensen, Phys. Rev. C **36**, 115 (1987).
[34] Y. Aritomo and M. Ohta, Nucl. Phys. **A753**, 152 (2005).
[35] A. Sandulesu and W. Greiner, Rep. Prog. Phys. **55**, 1423 (1992).
[36] W. Greiner, in *Proceeding of Fusion Dynamics at the Extremes, Dubna, Russia, 25–27 May 2000*, edited by Yu. Ts. Oganessian and V. I. Zagrebaev (World Scientific, Singapore, 2001), p. 1.